High-temperature superconductivity in heavily N- or B-doped graphene

Jian Zhou, Qiang Sun, Qian Wang, and Puru Jena

High-Temperature Superconductivity in Heavily N-(B-) Doped Graphene

Jian Zhou,[1,*] Qiang Sun,[2,3,1] Qian Wang,[3,2,1] Puru Jena[1,*]

[1]Department of Physics, Virginia Commonwealth University, Richmond, Virginia 23284, USA

[2]Department of Materials Science and Engineering, College of Engineering, Peking University, Beijing 100871, China

[3]Center for Applied Physics and Technology, College of Engineering, Peking University, Beijing 100871, China

Abstract

Two-dimensional honeycomb lattice of graphene, if heavily doped with electrons or holes, has been predicted to possess a wealth of fascinating properties including high temperature superconductivity. Although such a material is possible with high concentration of N- (or B-) substitution, its experimental realization has been hindered due to its dynamic instability. Using density functional theory combined with a global structural search and phonon dispersion calculations, we show that an ordered 50% N- (B-) doped graphene can be made energetically and dynamically stable by simultaneous doping carriers and applying biaxial tensile strain; carrier doping moves the system toward aromaticity while tensile strain reduces adverse effects associated with electrostatic interaction. Electron-phonon coupling calculations show that the N- (B-) doped graphene is superconducting with critical temperature reaching above the melting point of nitrogen in the case of 50% N-doped graphene. In addition, the ideal strength of N-doped graphene is even higher than that of pure graphene.

PACS: 63.22.Rc, 81.05.ue, 74.78.-w, 62.25.-g

---

[*] jzhou2@vcu.edu; pjena@vcu.edu

I. INTRODUCTION

The successful synthesis of graphene [1] has led to considerable interest in exploring two-dimensional (2D) electron behavior of honeycomb lattices. One fascinating property is high superconducting critical temperature T_c with unique topological behavior [2-10]. Note that pure graphene is not a good superconductor due to its vanishing density of states at the Fermi level (N_F), a consequence of point-like Fermi surface in the Brillouin zone. In addition, the effective electron pairing potential at the Fermi level (V_{ep}) is weak which results in very small electron-phonon coupling (EPC) parameter $\lambda = N_F V_{ep}$.

Currently there are two main strategies to enhance the EPC of graphene-based materials. The first one is surface functionalization – depositing metal atoms on graphene can make it superconducting [7-10]. Because enhancement of λ is related to metallic electrons around the Fermi level, such superconductivity is not intrinsic and the resulting T_c's are below 10 K. The second strategy is to introduce electrons or holes to graphene, especially heavy doping up to its Van Hove singularity point. Recent theoretical studies predicted that such a material would exhibit unconventional $d+id$-wave chiral superconductivity [5,6]. In addition, carrier doped graphene could possess T_c up to 30 K; even higher T_c can be expected if heavier carrier doping can be introduced [2]. Unfortunately, such heavy carrier doping concentration necessary to achieve such high T_c with unconventional properties not only has been experimentally unfeasible but also breaks the structure.

Note that since N (B) has one electron more (less) than C, substituting C in graphene by N (B) atoms is equivalent to electron (hole) doping. In addition, the Fermi level would move close to the Van Hove singularity if the dopant concentration is high. One can image that heavy substituting C in graphene with N (B) would behave in the same way. In spite of the tremendous efforts made during the past decade, the biggest experimental challenge in N-(or B-) substituted graphene without vacancy (keeping intact honeycomb lattice) is that the doping concentration is very *limited*. The maximum N content that has been achieved experimentally thus far is 21.66 wt%, corresponding to honeycomb-(h-) $C_{1-x}N_x$ composition of $x = 19.1\%$ [11]. Yakobson and oworkers used a cluster expansion model to explore the structure and stability of h-$C_{1-x}N_x$ with different x and concluded that when x exceeds 37.5%, the 2D alloy structure will be dynamically

unstable [12]. Similarly, in B-doped graphene (h-$C_{1-x}B_x$), the highest B uptake is $x = 25\%$, namely, BC_3 sheet [13,14].

In this study we propose a way to overcome this problem and realize heavily doped graphene with high superconducting temperature. We show that the synthesis of 50% N- (B-) doped graphene is possible by simultaneously introducing intermediate carriers and applying external strain. Our conclusion is based on density functional theory (DFT) calculations within the generalized gradient approximation (GGA) [15] combined with a global structural search and kinetic stability analysis. We further propose, based on formation energy calculations, that 50% N-doped graphene can be experimentally realized if s-triazine-C_3N_4 is used as a precursor. The ideal strength of h-CN is found to be high, namely 17.5%, thus outperforming pure graphene. Equally important, in these stable materials the Fermi level is found to be located near the Van Hove singularity. This is equivalent to heavily carrier doped graphene proposed previously. Electron-phonon calculations demonstrate that both the h-CN and h-CB are phonon-mediated superconductors, with the critical temperature, T_c of h-CN reaching as high as 66.8 K, above nitrogen's melting point.

II. COMPUTATIONAL METHODS

A. First-principles calculation

Our DFT/GGA calculations are carried out using norm-conserving pseudopotentials as implemented in Quantum-ESPRESSO code [16]. A plane-wave basis set with cutoff energy of 80 Ry is used. We also tested higher cutoff energy, but the results did not change. The Gaussian smearing scheme with smearing width of 0.01 Ry is applied for self-consistent calculations. Phonon dispersion matrix is calculated using density functional perturbation theory (DFPT) method [17]. We used vacuum space of 15 Å between different layers. A ($64\times64\times1$) uniform k-point mesh [18] and a ($8\times8\times1$) q-point grid are applied for electronic integration and phonon calculations, respectively. A much finer k-grid of ($96\times96\times1$) is adopted for the electron-phonon coupling (EPC) calculation. Carrier doping is simulated by using a uniform jellium counturcharge background to maintain charge neutrality. Formation energy and band structure calculations are repeated by using the Vienna *ab initio* simulation package (VASP) [19] with

projector augmented wave method [20]. The results are consistent with those obtained using the Quantum-ESPRESSO code.

B. Discrete particle-swarm optimization

First we explore the optimal geometry of 50% N-doped graphene by searching the globally minimum total energy configuration and then examining its dynamical stability. To do this, we apply an evolutionary discrete PSO algorithm combined with energy calculated at the DFT/GGA level of theory. The PSO algorithm has been well tested to predict the geometric structures [21]. In order to reduce periodic constraints, we adopt ($3\times3\times1$) and ($4\times4\times1$) supercells and search for the lowest energy of honeycomb C-N alloy with C:N = 1:1 in both its neutral and hole-doped states. In the global search for optimal structure, we adopt two hexagonal ($3\times3\times1$) and ($4\times4\times1$) supercells containing C_nN_n with $n = 9$ and 16, respectively, to reduce periodic constraints. In each supercell, we randomly generate M (=20) different 50% N-substituted graphene patterns as the initial generation. A vector of range $2n$ is used to denote each structure,

$$u_i^t = [x_{i,1}^t, x_{i,2}^t, ..., x_{i,2n}^t], \qquad i = 1, 2, ..., M . \tag{1}$$

In the vector, all the elements x are either 0 or 1, corresponding to the site occupied by C or N, respectively. DFT is then used to calculate the total energy and forces of each structure to locate the nearest local minimum on the potential energetic surface (PES). Starting from the next generation, we use PSO algorithm to surmount energy barriers on PES and approach lower-lying minima. In detail, we calculate the "velocity" of $x_{i,j}^t$,

$$v_{i,j}^{t+1} = \omega v_{i,j}^t + c_1 r_1 \left(\text{pbest}_{i,j}^t - x_{i,j}^t \right) + c_2 r_2 \left(\text{gbest}_j^t - x_{i,j}^t \right), \quad i = 1, 2, ..., M; \ j = 1, 2, ..., 2n , \tag{2}$$

where $v_{i,j}^t$ is the velocity from generation step $t - 1$ to t and r_1 and r_2 are random numbers in the range [0, 1]. The term $\text{pbest}_{i,j}^t$ is the element j value of the best (lowest energy) pattern that has been reached for particle i, and gbest_j^t is the element j value of the best pattern of all the particles. The inertial parameter ω linearly decreases from 0.9 to 0.4 during iteration. After obtaining the velocity of all elements j, we swap a few high velocity C ($x = 0$) and N ($x = 1$) pairs, to generate the new particle for the next generation. DFT optimization is again performed

for all the particles. After optimization, 40% (eight) structures with high energies are eliminated and replaced by random structures. This procedure is iterated for at least 20 cycles until the lowest energy structure remains unchanged for several generations.

III. RESULTS

A. Structure of 50% N-doped graphene

After the search, we obtain a disordered C-N alloy with some broken bonds in the neutral state, which is energetically much lower than the ordered h-CN alloy [Fig. 1(a)]. We then dope 0.3 holes in each unit cell (denoted as $p = 0.3$, corresponding to a concentration of 6.3×10^{14} cm^{-2}, comparable with experimentally achieved carrier concentration [22,23]), and repeated the search. This led to an ordered h-CN sheet having the lowest energy and indicating that hole-doping can energetically stabilize ordered h-CN [Fig. 1(b)].

$\Delta E = 0.00$ eV/CN $\qquad\qquad$ $\Delta E = 0.35$ eV/CN

(a)

$\Delta E = 0.00$ eV/CN $\qquad\qquad$ $\Delta E = 0.11$ eV/CN
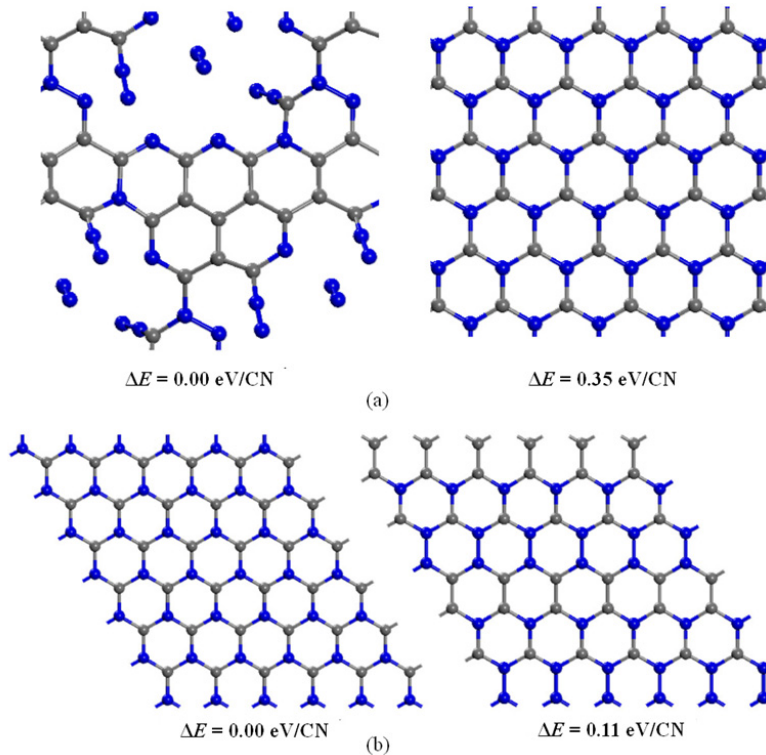
(b)

FIG. 1. Structure and relative energy of the lowest energy (left panel) and ordered pattern (right panel) state of h-CN in (a) neutral and (b) hole-doping ($p = 0.3$) state.

B. Dynamical stability of *h*-CN

Next we study its dynamical stability. In order to compare with previous results, we start by analyzing the ordered *h*-CN in its neutral state. In Fig. 1(a) we show its relaxed structure, with its equilibrium lattice constant L_0 and C-N bond length as 2.336 and 1.349 Å, respectively. Phonon dispersion calculation [Fig. 2(b)] shows two branches having imaginary frequency modes (following conventional notation, we plot imaginary frequency as negative values), consistent with previous results [12]. The lower soft branch corresponds to out-of-plane acoustic (ZA) mode, and the upper branch is out-of-plane optic (ZO) mode. These two soft modes indicate that the neutral *h*-CN is dynamically unstable, which is why it is difficult to synthesize.
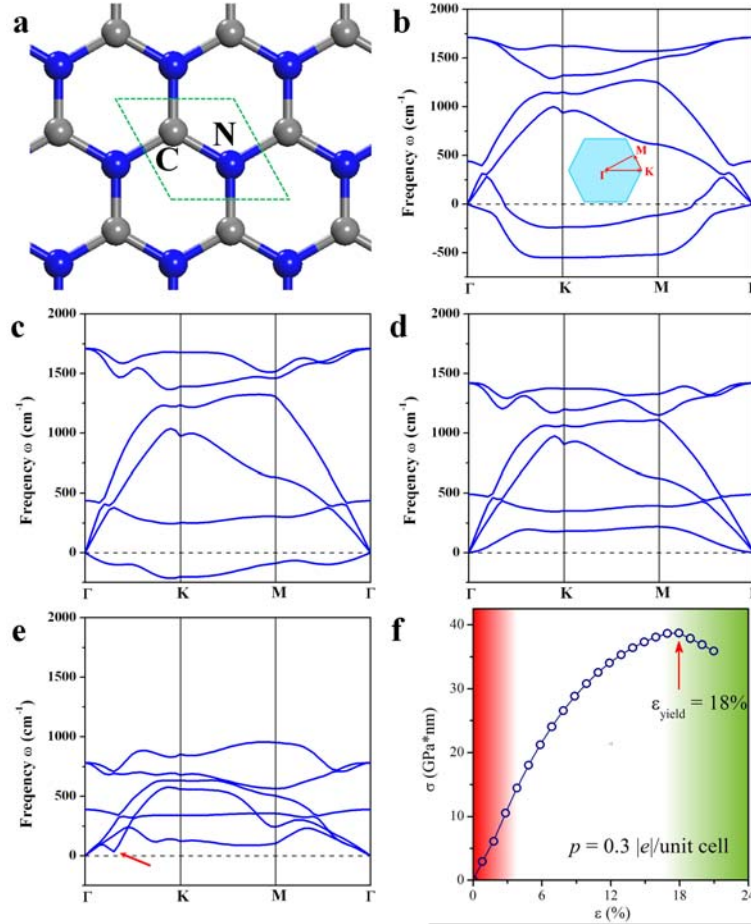

FIG. 2. (a) Structure of *h*-CN sheet with green dashed rhombus representing the unit cell. Phonon dispersion relations of *h*-CN in (b) neutral and strain-free state ($p = 0$, $\varepsilon = 0\%$), (c) hole-

6

doped and strain-free state ($p = 0.3$, $\varepsilon = 0\%$), (d) hole-doped and slightly stretched state ($p = 0.3$, $\varepsilon = 4.1\%$), (e) hole-doped and large strain state ($p = 0.3$, $\varepsilon = 17.5\%$). Inset in (b) shows high symmetry q-point path. In (f) we show strain-stress curve of h-CN in $p = 0.3$ state. Red (green) shaded area indicates electrostatic (Kohn anomaly) soft mode instability.

Since the dynamic instability arises from the surplus electrons on N atoms, we consider the effect of hole-doping on the phonon dispersion relation. We found that in the hole-doped ($p = 0.3$) state, the ZA mode remains imaginary, while the ZO mode becomes stable [Fig. 2(c)]. We calculate electron density difference between the hole-doped state and neutral state ($\Delta\rho = \rho_{p=0.3} - \rho_{neutral}$), which clearly shows that electrons are depleted mainly from the C and N nuclear sites [Fig. 3(a)]. This indicates that the electrons are removed from the anti-bonding state of the C-N bonds.
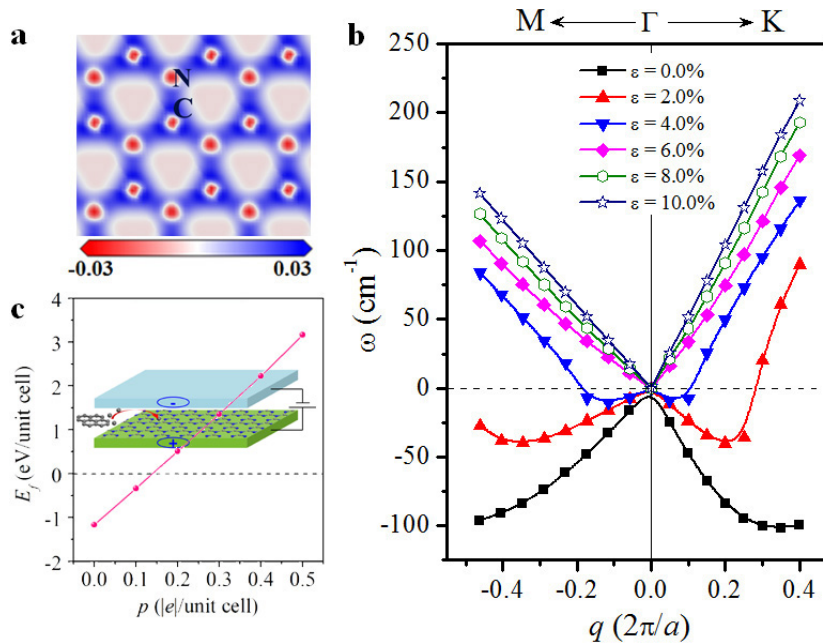

FIG. 3. (a) Slice form of electron difference $\Delta\rho$ (in $|e|/\text{Å}^3$). (b) Frequency shift near long wavelength limit under different strain ($p = 0.3$). In (c) we show the proposed experimental setup from s-triazine-C_3N_4 sheet to h-CN sheet with corresponding formation energy.

In order to raise the ZA branch, we apply a tensile strain ε along both *x* and *y* directions. As shown in Fig. 2(d), when ε = 4.1%, the *h*-CN sheet becomes dynamically stable as there are no more imaginary frequencies in the entire reciprocal space. In this way, the ordered *h*-CN is not only energetically the lowest state, but also it is dynamically stable. This result demonstrates that the N uptake concentration in graphene can be as high as 50% by applying both hole-doping and tensile strain, simultaneously. This concentration is much higher than that reported previously [11,12]. The strain induced ZA stabilization can be understood by considering a simple classical model which incorporates spring-like elastic force between nearest neighbor (C-N) atoms and electrostatic interactions among all C and N atoms. The total energy can be written as,

$$E_{\text{phonon}} = E_{\text{elastic}} + E_{\text{electrostatic}} = \frac{1}{2}\left(\frac{1}{2}\beta\sum_{\langle i,j\rangle}\left|\mathbf{r}_i - \mathbf{r}_j\right|^2 + \sum_{i,j}^{j\neq i}\frac{Q_iQ_j}{\left|\mathbf{r}_i - \mathbf{r}_j\right|}\right),$$ (3)

where *i* (*j*) is atom index, Q_i (Q_j) refers to its charge, $\mathbf{r}_i$ ($\mathbf{r}_j$) is its coordinate vector, β denotes stiffness of the spring, and the coefficient ½ is to avoid double counting between site *i* and *j*. Denoting the displacement along *z* direction of C and N atoms as $u_{\mathbf{n}}$ and $v_{\mathbf{n}}$, respectively (Figure S1 in Supplemental Material [24]), the equation of motion can be written as,

$$M_1\ddot{u}_{\mathbf{n}} = \sum_{\mathbf{p}}C_{R,\mathbf{p}}^{\text{C}}\left(u_{\mathbf{n}+\mathbf{p}} - u_{\mathbf{n}}\right) - \sum_{\mathbf{p}}C_{A,\mathbf{p}}\left(v_{\mathbf{n}+\mathbf{p}} - u_{\mathbf{n}}\right) + \beta\sum_{\mathbf{r}}\left(v_{\mathbf{n}+\mathbf{r}} - u_{\mathbf{n}}\right),$$

$$M_2\ddot{v}_{\mathbf{n}} = \sum_{\mathbf{p}}C_{R,\mathbf{p}}^{\text{N}}\left(v_{\mathbf{n}+\mathbf{p}} - v_{\mathbf{n}}\right) - \sum_{\mathbf{p}}C_{A,\mathbf{p}}\left(u_{\mathbf{n}+\mathbf{p}} - v_{\mathbf{p}}\right) + \beta\sum_{\mathbf{r}}\left(u_{\mathbf{n}-\mathbf{r}} - v_{\mathbf{n}}\right),$$ (4)

where M_1 and M_2 are mass of C and N atom, respectively. Vectors $\mathbf{r}$ and $\mathbf{p}$ link the atom under study to its nearest and second nearest neighbor atoms (Figure S1 in Supporting Information), respectively, which take form

$$\mathbf{p} = l\mathbf{a}_1 + m\mathbf{a}_2 \quad (l,m \in \Box)$$
$$\mathbf{r} = \mathbf{0}, \ \mathbf{a}_1, \ \mathbf{a}_2$$, (5)

Here $\mathbf{a}_1$ and $\mathbf{a}_2$ are two-dimensional real space crystal lattice vectors (*L* is lattice constant). After solving this equation in the long wavelength limit $\mathbf{q} = \eta_1\hat{\mathbf{G}}_1 + \eta_2\hat{\mathbf{G}}_2$ (see Supporting Information), we find that the stability of ZA mode is determined by the value of a dimensionless scaling

parameter $\gamma = \bar{Q}^2/\beta L^3 > 0$, where $\bar{Q} = \sqrt{|Q_N||Q_C|}$. When γ is large, the electrostatic interaction dominates and the ZA mode is unstable in the long wavelength limit. On the other hand, if we apply a tensile strain to increase the lattice constant L, γ can be reduced and the long wavelength ZA mode then becomes positive. This tendency agrees well with our DFPT results which show that larger biaxial tension moves the ZA mode upward [Fig. 3(b)]. We also see that under small ε (4%), the ZA mode has quadratic dispersion with respect to $\mathbf{q}$ ($\omega \sim q^2$) in the vicinity of Γ. When ε exceeds 8%, this relationship becomes linear ($\omega \sim q$), consistent with the results in stretched graphene [25].

We now apply large tensile strain to study the ideal strength of hole-doped h-CN sheet, which is a very important mechanical property of a nanomaterial. As shown in Fig. 2(e), no phonon softening appears at $\varepsilon = 17.5\%$, but there is a mode on the Γ-K path whose frequency is approaching zero as ε increases and becomes imaginary at $\varepsilon = 17.6\%$. This phonon-dominated instability is associated with Kohn anomaly [26] which will be discussed in the following. We also calculate stress-strain curve which shows no structural instability before the Kohn anomaly sets in (yield point at $\varepsilon = 18\%$) [Fig. 2(f)]. Hence, the critical strain of hole-doped h-CN can be as high as 17.5%, which is larger than that of pristine graphene, namely, 14.5% [27], as well as carrier strengthened graphene [28]. In Table I we list the minimum and maximum strain to stabilize h-CN under different hole-doping levels.

Table I. Minimum (ε_{min}) and maximum (ε_{max}) strain required to stabilize h-CN.

p	0.2	0.3	0.4	0.5
ε_{min}	6.3%	4.1%	4.8%	7.0%
ε_{max}	15.1%	17.5%	15.6%	13.7%

We now suggest a possible route to synthesize the ordered h-CN. We begin with an experimentally fabricated s-triazine-C_3N_4 sheet [29] as a precursor. By depositing it on a selected substrate and applying a back gate voltage, it is easy to make the s-triazine-C_3N_4 sheet slightly

stretched and hole-doped. We calculate the formation energy E_f of embedding C atoms into s-triazine-C$_3$N$_4$ to synthesize a h-CN sheet, using the lattice constant of h-CN sheet consistent with 10% tensile strain [Fig. 3(c)]. The formation energy per CN under different p-doping level reads

$$E_f^p = \left(\mu_C + E_{C_3N_4}^p - E_{C_4N_4}^p \right) / 4 , \tag{6}$$

where the chemical potential, μ_C of carbon atom is same as that in the graphene sheet. $E_{C_3N_4}^p$ [$E_{C_4N_4}^p$] is the total energy of s-triazine-C$_3$N$_4$ in one unit cell [h-CN in a ($2\times2\times1$) supercell]. We see that in neutral and low doping states, E_f is negative, indicating endothermic reaction. When the doping level, p, is increased to 0.3, E_f becomes positive and increases linearly with p, hence the reaction is exothermic, making it experimentally achievable.

C. Electronic structure of h-CN

Next we examine its electronic properties. As seen in Fig. 4(a), the system shows an n-doped semiconducting behavior with the Fermi level located near the Van Hove singularity at the M point of the Brillouin zone. This is consistent with the previously proposed heavily electron doped graphene with 5/8 filling of the π band. Thus, we can expect the theoretically predicted unconventional chiral $d+id$-wave superconducting state in a *real* material [5,6]. In the band structure, we use different color to represent the atomic contribution of each state. Here blue (red) color represents the state contributed solely by N (C) atom. The band I is mainly from the N atoms, while the band II is mainly from the C atoms. These results are consistent with the projected density of state (PDOS) results. Furthermore, we calculate maximally localized Wannier functions (MLWFs) [30] of these two bands [Fig. 3(c) and 3(d)], and observe that they have p_z-orbital characteristics. Hence, these two band dispersions can be repeated by a simplified tight binding (TB) model

$$\hat{H} = -t \sum_{\langle i,j \rangle} \hat{c}_i^\dagger \hat{c}_j + \frac{\Delta}{2} \sum_i (-1)^i \, \hat{c}_i^\dagger \hat{c}_i , \tag{7}$$

where t is hopping integral between nearest neighbor i and j sites, and Δ is the on-site energy difference between the C and N sites with $(-1)^i = +1$ (-1) for C (N). By fitting the TB band

structure with the DFT results, we plot the variation of t and Δ under different tensile strains [Fig. 4(b)]. Note that both t and Δ decrease linearly with increasing strain. Therefore, under larger tension, the electron hopping between C and N becomes harder, while the on-site energy difference between them becomes smaller. In Figure 4e we plot the simulated scanning tunneling microscope (STM) image of the system.
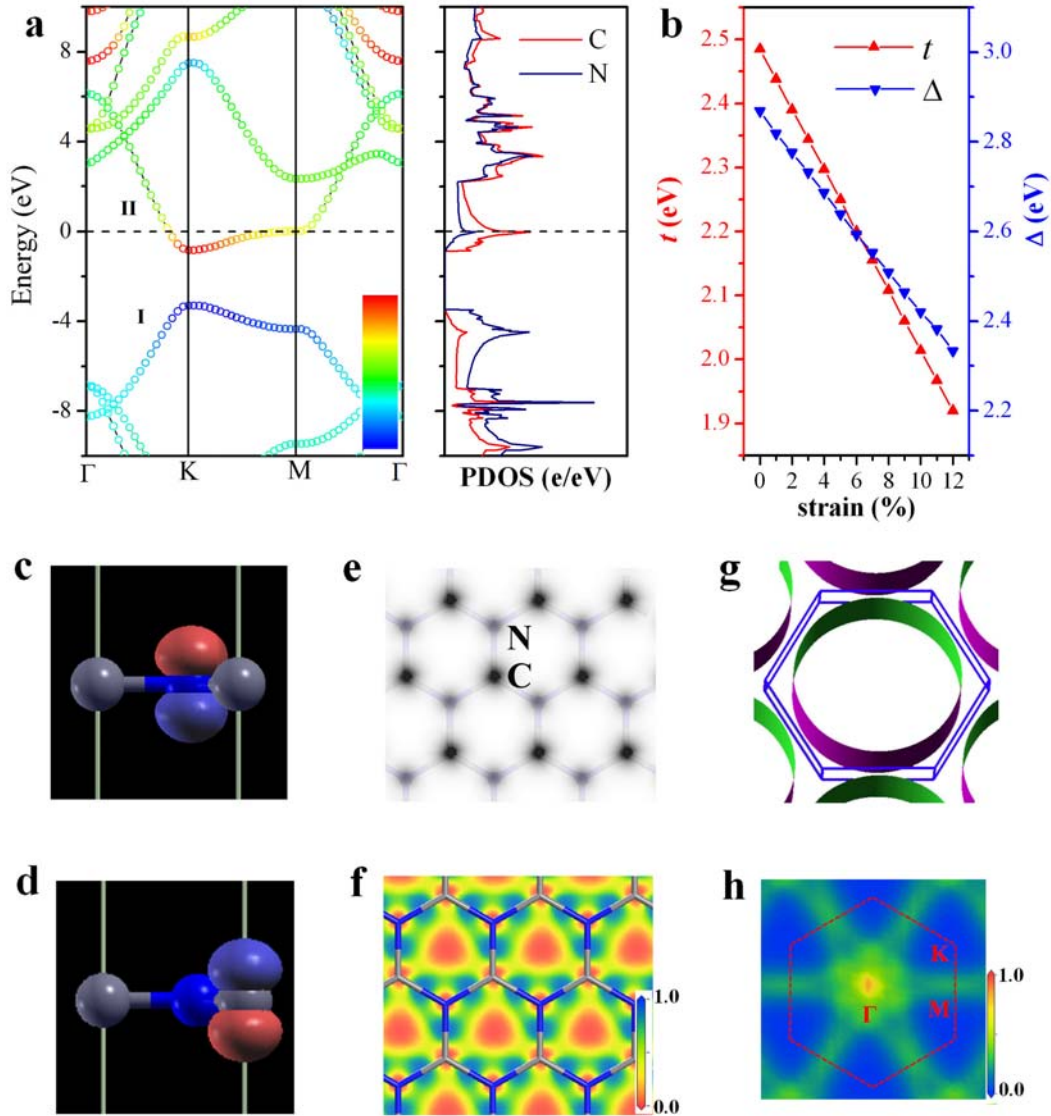

FIG. 4. (a) Band structure and PDOS of h-CN sheet with $p = 0.3$ and $\varepsilon = 10\%$. Blue (red) color represents the state contributed by N (C) atom. (b) Variation of t and Δ under different strain. (c) and (d) MLWFs of band I and II with p_z characteristics. Slice form of (e) simulated STM image and (f) ELF of the system. (g) Fermi surface pocket and (h) nesting function $X_{\mathbf{q}}$.

To further understand the bonding feature of hole-doped *h*-CN sheet, we calculate the valence electron localization function (ELF) of the system with $p = 0.3$ and $\varepsilon = 10\%$. ELF is widely used to describe the spatial distribution of electrons, which is normalized from 0.0 to 1.0 [31]. The values of 0.5 and 1.0 represent fully delocalized and fully localized state, respectively. From Fig. 4(f), we see that the delocalized electrons (yellow color) distribute around C and N atoms, which are connected with each other in the whole sheet. On the C-N bond, the electrons are localized forming a bonding state.

We now reveal the geometrical structure of its Fermi surface [Fig. 4(g)], where we see an isotropic Fermi (electron) pocket in the *xy* plane near the M point of the Brillouin zone. We accordingly calculate the nesting function [Fig. 4(h)],

$$X_{\mathbf{q}} = \sum_{\mathbf{k},m,n} \delta\left(E_{m,\mathbf{k}+\mathbf{q}} - E_{\mathrm{F}}\right) \delta\left(E_{n,\mathbf{k}} - E_{\mathrm{F}}\right). \tag{8}$$

Non-zero $X_{\mathbf{q}}$ indicates that there are two states on the Fermi surface, $\mathbf{k}$ and $\mathbf{k}'$, with $\mathbf{q} = \mathbf{k}' - \mathbf{k}$. Larger $X_{\mathbf{q}}$ indicates more electron states are connected between $\mathbf{k}$ and $\mathbf{k}'$. We see that in the hole-doped *h*-CN, non-zero $X_{\mathbf{q}}$ distributes mainly around Γ and along $\Gamma \rightarrow M$ path. At the non-zero $X_{\mathbf{q}}$ points, the screening effects of electrons in a metal can strongly change atomic vibrations, and the vibration frequencies ω vary abruptly with $\mathbf{q}$, a signature of Kohn anomaly instability. Our $X_{\mathbf{q}}$ plot agrees well with the phonon dispersion calculation where the Kohn anomaly occurs at the vicinity of the Γ point.

D. Superconductivity of *h*-CN

Now we estimate its phonon-mediated superconducting transition temperature by calculating the Eliashberg function $\alpha^2 F(\omega)$, EPC parameter λ, and the logarithmic frequency average ω_{log}. Using Allen–Dynes modified McMillan equation [32,33]

$$T_c = \frac{\hbar \omega_{\mathrm{log}}}{1.2 k_{\mathrm{B}}} \exp\left[\frac{-1.04(1+\lambda)}{\lambda - \mu^*(1+0.62\lambda)}\right], \tag{9}$$

with a typical value of 0.115 for the effective Coulomb repulsion parameter μ^*, we calculate the critical superconducting temperature T_c of stable h-CN under hole-doping and tensile strain. We systematically calculate ω_{log}, λ, and T_c of 10% stretched h-CN under different carrier doping conditions. Similar to the graphene case,[2] higher carrier concentration yields smaller ω_{log} and larger λ [Fig. 5(a)]. Hence T_c increases from 0.2 K ($p = 0.2$, $\varepsilon = 10\%$) to 46.5 K ($p = 0.5$, $\varepsilon = 10\%$) [Fig. 5(b)]. Since large tension also enhances EPC [2], we calculate T_c for each doping configuration under its maximum tension. The results are shown as empty diamond points in Fig. 5(b). The highest T_c among them appears for h-CN with $p = 0.4$ and $\varepsilon = 15.6\%$. Here, the dominant peak of $\alpha^2F(\omega)$ appears at $\omega \sim 200$ cm^{-1}, mainly from ZA modes, and contributes most of EPC [Fig. 5(c)]. The logarithmic frequency average ω_{log} and critical temperature T_c are found to be 362.8 K and 66.8 K, respectively. This T_c value is much higher than that in the conventional MgB$_2$ (39 K) and is above nitrogen's melting point (63.15 K).
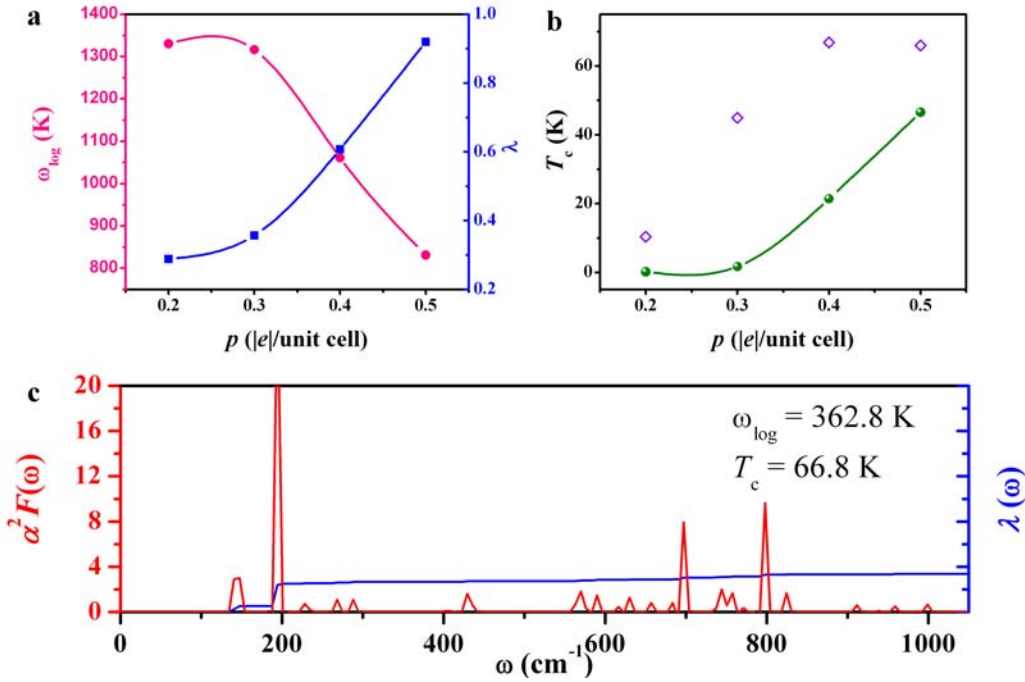

FIG. 5. (a) Variation of ω_{log} and $\lambda(\omega)$ with different doping level under 10% tension. (b) Calculated T_c with different doping level of h-CN sheet. Solid dot: under 10% tension, empty diamond: under maximum tension. (c) Calculated $\alpha^2F(\omega)$ and $\lambda(\omega)$ of h-CN sheet under $p = 0.4$ and $\varepsilon = 15.6\%$.

E. Stability and superconductivity of *h*-CB

In addition to N-doped graphene, we also consider a similar 50% B-doped graphene (*h*-CB) (Fig. 6). The equilibrium lattice constant of *h*-CB is optimized to be 2.677 Å. Similarly, this *h*-CB is dynamically unstable in its neutral state (TA soft mode near Γ and ZA soft mode near Γ and M in the Brillouin zone), due to lack of electrons of B atoms. However, if we add some electrons ($n = -0.2$ $|e|$/unit cell, corresponding to a donor concentration of 3.2×10^{14} cm^{-2}) and apply a biaxial tensile strain ($\varepsilon = 5\%$), the system becomes dynamically stable without imaginary frequencies. This shows that carrier doping and tensile strain applied simultaneously can also stabilize a highly B-doped graphene. Band structure calculations show that the *h*-CB is metallic with the Fermi level located near the Van Hove singularity [24]. Strong electron-phonon interactions (Fig. 7) are also found that lead to $T_c = 44.4$ ($n = -0.2$, $\varepsilon = 5\%$) and 40.4 K ($n = -0.3$, $\varepsilon = 5\%$), again higher than that of MgB$_2$.
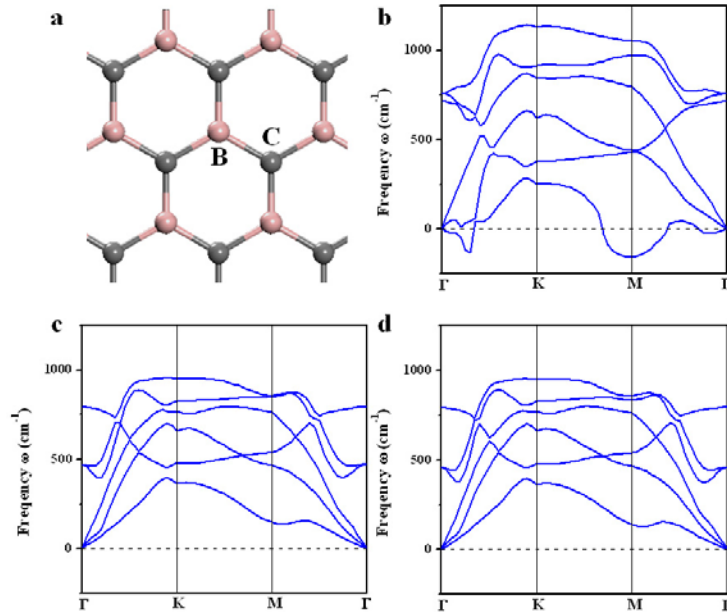

FIG. 6. (a) Geometrical structure of the *h*-BC sheet. Phonon dispersion of *h*-BC in (b) neutral and strain free state, (b) $n = -0.2$ $|e|$/unit cell, $\varepsilon = 5\%$ state, and (c) $n = -0.3$ $|e|$/unit cell, $\varepsilon = 5\%$ state.
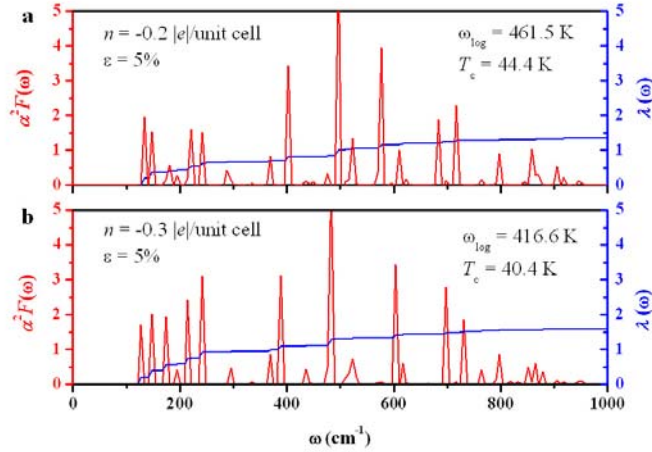
FIG. 7. Eliashberg function $\alpha^2F(\omega)$ and $\lambda(\omega)$ of h-BC under (a) $n = -0.2$ $|e|$/unit cell, $\varepsilon = 5\%$ state, and (b) $n = -0.3$ $|e|$/unit cell, $\varepsilon = 5\%$ state. The critical temperatures T_c are estimated to be 44.4 K and 40.4 K, respectively.

IV. CONCLUSION

In summary, we propose a pathway to synthesize heavily carrier doped graphene with an unconventional high T_c superconducting state. Our study of 50% N- (B-) doped graphene leads to the following conclusions: (*i*) In its neutral state, the ordered h-CN is unstable with imaginary frequencies in ZA and ZO modes. Hole-doping can stabilize the ZO mode by removing electrons from the anti-bonding state while tensile strain can stabilize the ZA mode by weakening electrostatic interaction between C and N. (*ii*) The h-CN can withstand tension as high as 17.5%, thus, outperforming graphene. (*iii*) Hole-doped ordered h-CN is energetically favorable among all the N-doped graphene systems. By calculating the formation energy, we propose that a hole-doped and stretched s-triazine-C_3N_4 can be used as a precursor to fabricate h-CN experimentally. (*iv*) The h-CB sheet can similarly be stabilized with electron-doping and applied tensile strain. (*v*) With the Fermi level lying near the Van Hove singularity point, both h-CN and h-CB are metallic and phonon-mediated superconductors with critical temperatures reaching 66.8 K and 44.4 K, respectively. These stable and experimentally realizable materials provide a platform to verify and study the theoretically predicted unconventional superconductivity of heavily doped

graphene. The stabilization strategy can also be applied to other unstable 2D nanomaterials such as h-B sheet [34,35], 1T-MoS$_2$ [36], planar arsenene [37] and h-GaBi [38].

References:

1 K. S. Novoselov, A. K. Geim, S. V. Morozov, D. Jiang, Y. Zhang, S. V. Dubonos, I. V. Grigorieva, and A. A. Filrsov, Science **306**, 666 (2004).

2 C. Si, Z. Liu, W. Duan, and F. Liu, Phys. Rev. Lett. **111**, 196802 (2013).

3 H.-M. Zhang, Y. Sun, W. Li, J.-P. Peng, C.-L. Song, Y. Xing, Q. Zhang, J. Guan, Z. Li, Y. Zhao, S. Ji, L. Wang, K. He, X. Chen, L. Gu, L. Ling, M. Tian, L. Li, X. C. Xie, J. Liu, H. Yang, Q.-K. Xue, J. Wang, and X. Ma, Phys. Rev. Lett. **114**, 107003 (2015).

4 N. B. Kopnin and E. B. Sonin, Phys. Rev. Lett. **100**, 246808 (2008).

5 R. Nandkishore, L. S. Levitov, and A. V. Chubukov, Nat. Phys. **8**, 158 (2012).

6 M. L. Kiesel, C. Platt, W. Hanke, D. A. Abanin, and R. Thomale, Phys. Rev. B **86**, 020507(R) (2012).

7 G. Profeta, M. Calandra, and F. Mauri, Nat. Phys. **8**, 131 (2012).

8 J. L. McChesney, A. Bostwick, T. Ohta, T. Seyller, K. Horn, J. González, and E. Rotenberg, Phys. Rev. Lett. **104**, 136803 (2010).

9 J. Zhou, Q. Sun, Q. Wang, and P. Jena, Phys. Rev. B **90**, 205427 (2014).

10 J. Zhou, S. Zhang, Q. Wang, Y. Kawazoe, and P. Jena, Nanoscale **7**, 2352 (2015).

11 S. Zhang, S. Tsuzuki, K. Ueno, K. Dokko, and M. Watanabe, Angew. Chem. Int. Ed. **54**, 1302 (2015).

12 Z. Shi, A. Kutana, and B. I. Yakobson, J. Phys. Chem. Lett. **6**, 106 (2015).

13 H. Yanagisawa, T. Tanaka, Y. Ishida, E. Rokuta, S. Otani, and C. Oshima, Phys. Rev. B **73**, 045412 (2006).

14 X. Luo, J. Yang, H. Liu, X. Wu, Y. Wang, Y. Ma, S.-H. Wei, X. Gong, and H. Xiang, J. Am. Chem. Soc. **133**, 16285 (2011).

15 J. P. Perdew, K. Burke, and M. Ernzerhof, Phys. Rev. Lett. **77**, 3865 (1996).

16 P. Giannozzi, S. Baroni, N. Bonini, M. Calandra, R. Car, C. Cavazzoni, D. Ceresoli, G. L. Chiarotti, M. Cococcioni, I. Dabo, A. Dal Corso, S. Fabris, G. Fratesi, S. de Gironcoli, R. Gebauer, U. Gerstmann, C. Gougoussis, A. Kokalj, M. Lazzeri, L. Martin-Samos, N. Marzari, F. Mauri, R. Mazzarello, S. Paolini, A. Pasquarello, L. Paulatto, C. Sbraccia, S. Scandolo, G. Sclauzero, A. P. Seitsonen, A. Smogunov, P. Umari, and R. M. Wentzcovitch, J. Phys: Condens. Matter **21**, 395502 (2009).

17 S. Baroni, S. de Gironcoli, A. Dal Corso, and P. Giannozzi, Rev. Mod. Phys. **73**, 515 (2001).

18 H. J. Monkhorst and J. D. Pack, Phys. Rev. B **13**, 5188 (1976).

19 G. Kresse and J. Furthmuller, Phys. Rev. B **54**, 11169 (1996).

20 G. Kresse and J. Joubert, Phys. Rev. B **59**, 1758 (1999).

21 Y. Wang, J. Lv, L. Zhu, and Y. Ma, Phys. Rev. B **82**, 094116 (2010).

22 P. Moetakef, J. R. Williams, D. G. Ouellette, A. P. Kajdos, D. Goldhaber-Gordon, S. James Allen, and S. Stemmer, Phys. Rev. X **2**, 021014 (2012).

23 D. K. Efetov and P. Kim, Phys. Rev. Lett. **105**, 256805 (2010).

24 See Supplemental Material at [URL] for Model of tensile strain for stabilizing the phonon dispersion and electronic structure of 50% B-doped graphene.

25 F. Liu, P. Ming, and J. Li, Phys. Rev. B **76**, 064120 (2007).

26 W. Kohn, Phys. Rev. Lett. **2**, 393 (1959).

27 C. A. Marianetti and H. G. Yevick, Phys. Rev. Lett. **105**, 245502 (2010).

28 C. Si, W. Duan, Z. Liu, and F. Liu, Phys. Rev. Lett. **109**, 226802 (2012).

29 X. Wang, K. Maeda, A. Thomas, K. Takanabe, G. Xin, J. M. Carlsson, K. Domen, and M. Antonietti, Nat. Mater. **8**, 76 (2009).

30 A. A. Mostofi, J. R. Yates, Y.-S. Lee, I. Souza, D. Vanderbilt, and N. Marzari, Comput. Phys. Commun. **178**, 685 (2008).

31 A. D. Becke and K. E. Edgecombe, J. Chem. Phys. **92**, 5397 (1990).

32 W. L. McMillan, Phys. Rev. **167**, 331 (1967).

33 P. B. Allen and R. Dynes, Phys. Rev. B **12**, 905 (1975).

34 S.-Y. Xie, X.-B. Li, W. Q. Tian, N.-K. Chen, X.-L. Zhang, Y. Wang, S. Zhang, and H.-B. Sun, Phys. Rev. B **90**, 035447 (2014).

35 L. Z. Zhang, Z. F. Wang, S. X. Du, H.-J. Gao, and F. Liu, Phys. Rev. B **90**, 161402(R) (2014).

36 S. N. Shirodkar and U. V. Waghmare, Phys. Rev. Lett. **112**, 157601 (2014).

37 C. Kamal and M. Ezawa, Phys. Rev. B **91**, 085423 (2015).

38 L. Li, X. Zhang, X. Chen, and M. Zhao, Nano Lett. **15**, 1296 (2015).